Imposing Dirichlet boundary conditions in the eXtended Finite Element method

Nicolas Moes, Eric Béchet, Matthieu Tourbier

Imposing Dirichlet boundary conditions in the extended finite element method

Nicolas Moës[1, *, †], Eric Béchet[2, ‡] and Matthieu Tourbier[1, §]

[1]*GeM Institute, Ecole Centrale de Nantes, Université de Nantes, CNRS, 1 Rue de la Noe, 44321 Nantes, France*

[2]*LPMM, UMR CNRS 7554, Université de Metz, Ile du Saulcy, 57045 Metz Cedex 1*

This paper is devoted to the imposition of Dirichlet-type conditions within the extended finite element method (X-FEM). This method allows one to easily model surfaces of discontinuity or domain boundaries on a mesh not necessarily conforming to these surfaces. Imposing Neumann boundary conditions on boundaries running through the elements is straightforward and does preserve the optimal rate of convergence of the background mesh (observed numerically in earlier papers). On the contrary, much less work has been devoted to Dirichlet boundary conditions for the X-FEM (or the limiting case of stiff boundary conditions). In this paper, we introduce a strategy to impose Dirichlet boundary conditions while preserving the optimal rate of convergence. The key aspect is the construction of the correct Lagrange multiplier space on the boundary. As an application, we suggest to use this new approach to impose precisely zero pressure on the moving resin front in resin transfer moulding (RTM) process while avoiding remeshing. The case of inner conditions is also discussed as well as two important practical cases: material interfaces and phase-transformation front capturing.

KEY WORDS: X-FEM; locking; inf–sup test; Lagrange multipliers; Dirichlet

1. INTRODUCTION

Imposing Dirichlet-type boundary conditions in the finite element framework is quite straightforward. For instance, these can be imposed directly by an appropriate L^2 projection on the boundary or by using Lagrange multipliers. The proper choice of the Lagrange multiplier space and subsequent integration of the bilinear form is well understood, see, for instance,

*Correspondence to: Nicolas Moës, GeM Institute, Ecole Centrale de Nantes, Université de Nantes, CNRS, 1 Rue de la Noe, 44321 Nantes, France.

†E-mail: nicolas.moes@ec-nantes.fr

‡E-mail: eric.bechet@univ-metz.fr

§E-mail: matthieu.tourbier@insa-rouen.fr

Contract/grant sponsor: French Ministry of Research

Reference [1] or [2]. The key issue is the verification of the so-called LBB condition. This condition is usually impossible to prove analytically and one can use instead a robust numerical test like the one designed by Chapelle and Bathe [3].

Regarding meshless methods, a lot of attention has been devoted recently to the imposition of Dirichlet boundary conditions. See, for instance, Reference [4] for the latest development on the topic or Reference [5] for an earlier reference. As often noted, the difficulty with meshless methods is that the shape functions do not satisfy the Kronecker delta property, i.e. the shape function emanating from a node does not vanish at all other nodes, unlike standard finite element shape functions.

The extended finite element method (X-FEM) uses regular finite element shape functions and adds new ones by an enrichment procedure known as the partition of unity technique [6]. The additional shape functions are introduced to model discontinuities inside the elements. The discontinuities may be related to cracks [7, 8], material interfaces [9, 10] or voids [11]. More precisely, in the case of voids, no enrichment is needed: the linear and bilinear forms are simply integrated in the non-void part of the elements. Also, nodes for which the support is completely in the void are eliminated. The X-FEM has proved to be successful to solve several important mechanical models for which a classical finite element failed (or lacked robustness) because of meshing issues. For instance, 3D complex cracks were grown without remeshing [12], homogenization was carried out on very complex micro-structures [10] or phase-transformation fronts were captured with no remeshing [13, 14]. Regarding the location and evolution of the physical surfaces, these are given in terms of a level set representation.

In this paper, we focus on imposing Dirichlet-type boundary conditions on stationary or evolving surfaces. In the meshless framework, the difficulty arises from the fact that the shape functions do not form the basis for an interpolation. In the X-FEM framework, the difficulty arises from the fact that there is no unique way to strongly impose Dirichlet boundary conditions. To illustrate this on a simple case, consider the mesh in Figure 1. The domain of interest Ω is not entirely matched by the mesh. How can one impose a value, say zero, on Γ? For instance, to have a zero value at point C, values at nodes A and B simply need to be opposite (we assume Γ runs through the middle of the last layer of elements). A closer look shows that for the interpolation to meet zero on Γ, the layer of nodes right above Γ must be set to the same value and all the nodes below Γ must be set to the same opposite value. The normal flux of the interpolation is thus constant along Γ which is not really satisfactory.

This simple example demonstrates, first, that there is no unique way to impose strongly Dirichlet boundary conditions in the X-FEM and, second, that the normal flux of the resulting interpolation is quite poor on the boundary ('boundary locking' occurs). The purpose of this paper is to show how to relax the strong imposition of the Dirichlet conditions while preserving the optimal rate of convergence of all variables on Γ and in Ω.

This paper will also deal with internal interfaces. To model continuity of displacements but discontinuity of strains, one approach is to enrich the continuous classical finite element base with a continuous (but strain discontinuous) function. A proper choice of the enrichment function gives an optimal rate of convergence as shown numerically in Reference [10]. Another tempting approach is to enrich the material interface with a discontinuous Heaviside function (as if it were a crack) and then saw together both sides with Lagrange multipliers, following the idea initiated by Merle and Dolbow [15]. This second approach involving Lagrange multipliers is the only one that extends easily to more complex non-linear constitutive laws on the interface (contact, debonding, etc.).

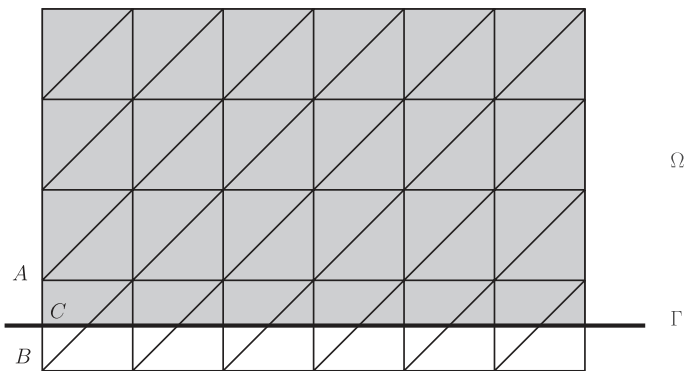

Figure 1. A domain of interest Ω (shaded area) located on a mesh not matching the Dirichlet boundary Γ of Ω.

The difficulty of choosing the proper Lagrange multiplier space to enforce interfacial constraints in the X-FEM framework was already observed by Ji and Dolbow [16]. The authors showed that a naive construction of the Lagrange multiplier space leads to oscillations in the multiplier. The proposed Lagrange multiplier space in this paper removes the oscillations.

Finally, note that the enforcement of interfacial or Dirichlet constraints is feasible using a Nitsche-type approach [17–19]. The two main advantages of the proposed approach over Nitsche's are the absence of a stability parameter and the straightforward extension to non-linear bulk behaviours.

2. DIRICHLET AND STIFF ROBIN LINEAR BOUNDARY CONDITIONS

2.1. The model problem

The model problem in this section is a 2D Laplace problem already considered in Reference [4]. The problem is defined over a unit-square and the exact solution is given by

$$u(x, y) = [\cosh(\pi y) - \coth(\pi)\sinh(\pi y)]\sin(\pi x) \tag{1}$$

and is shown in Figure 2.

The strong form set of equations is given by

$$\begin{cases} \Delta u = 0 & (x, y) \in \Omega :=]0, 1[\times]0, 1[\\ u = u_{\mathrm{D}} & (x, y) \in \Gamma_{\mathrm{D}} \\ \nabla_n u = t_{\mathrm{N}} & (x, y) \in \Gamma_{\mathrm{N}} \end{cases} \tag{2}$$

As shown in Figure 2, Dirichlet boundary conditions, u_{D}, are imposed on the lower side of the square domain whereas Neumann boundary conditions are imposed on the three other sides (∇_n is the outward directional derivative operator and t_{N} the (exact) imposed flux). The imposed Dirichlet and Neumann boundary conditions are in agreement with the analytical solution (1).

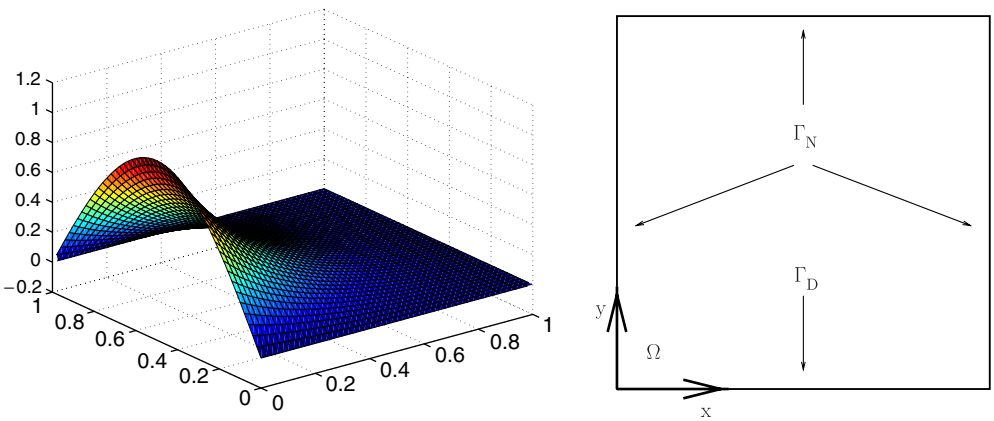

Figure 2. The exact solution of the 2D Laplace model problem (left) and the boundary conditions (right).

Let us now transform the strong form to a variational setting. Let $\mathscr{U}$ be the space of regular enough fields ($H^1(\Omega)$) and let $\mathscr{U}_D$ and $\mathscr{U}_0$ be the two subsets of $\mathscr{U}$ defined by

$$\mathscr{U}_D = \{u \in \mathscr{U} : u = u_D \text{ on } \Gamma_D\} \tag{3}$$

$$\mathscr{U}_0 = \{u \in \mathscr{U} : u = 0 \text{ on } \Gamma_D\} \tag{4}$$

The one-field variational formulation 'equivalent' to (2) is

$$\text{Find } u \in \mathscr{U}_D : \int_\Omega \nabla u \cdot \nabla v \, d\Omega = \int_{\Gamma_N} t_N v \, d\Gamma \quad \forall v \in \mathscr{U}_0 \tag{5}$$

Introducing a Lagrange multiplier, λ, to impose the Dirichlet boundary condition on Γ_D, we may write the following two-field variational formulation [1]:

$$\text{Find } u \in \mathscr{U}, \lambda \in \mathscr{L}: \tag{6}$$

$$\int_\Omega \nabla u \cdot \nabla v \, d\Omega - \int_{\Gamma_D} \lambda v \, d\Gamma = \int_{\Gamma_N} t_N v \, d\Gamma \quad \forall v \in \mathscr{U} \tag{7}$$

$$-\int_{\Gamma_D} \mu u \, d\Gamma = -\int_{\Gamma_D} \mu u_D \, d\Gamma \quad \forall \mu \in \mathscr{L} \tag{8}$$

where $\mathscr{L}$ is the space of Lagrange multipliers defined on the Dirichlet boundary. The discretization of the variational principle (8) involves the design of the finite element subspaces $\mathscr{U}^h \subset \mathscr{U}$ and $\mathscr{L}^h \subset \mathscr{L}$ leading to the discrete formulation:

$$\text{Find } u^h \in \mathscr{U}^h, \lambda^h \in \mathscr{L}^h: \tag{9}$$

$$\int_\Omega \nabla u^h \cdot \nabla v \, \mathrm{d}\Omega - \int_{\Gamma_\mathrm{D}}^{\mathrm{num}} \lambda^h v \, \mathrm{d}\Gamma = \int_{\Gamma_\mathrm{N}}^{\mathrm{num}} t_\mathrm{N} v \, \mathrm{d}\Gamma \quad \forall v \in \mathscr{U}^h \tag{10}$$

$$- \int_{\Gamma_\mathrm{D}}^{\mathrm{num}} \mu u^h \, \mathrm{d}\Gamma = - \int_{\Gamma_\mathrm{D}}^{\mathrm{num}} \mu u_\mathrm{D} \, \mathrm{d}\Gamma \quad \forall \mu \in \mathscr{L}^h \tag{11}$$

The symbol $\int^{\mathrm{num}}$ indicates that numerical under-integration of the corresponding terms may be used. To be even more general, let us consider that the Dirichlet conditions is replaced by the following Robin-type condition:

$$\lambda = -k(u - u_\mathrm{D}) \quad \text{on } \Gamma_\mathrm{D} \tag{12}$$

As k goes to infinity, we recover a Dirichlet-type condition. The discrete variational principle now reads as

$$\text{Find } u^h \in \mathscr{U}^h, \lambda^h \in \mathscr{L}^h: \tag{13}$$

$$\int_\Omega \nabla u^h \cdot \nabla v \, \mathrm{d}\Omega - \int_{\Gamma_\mathrm{D}}^{\mathrm{num}} \lambda^h v \, \mathrm{d}\Gamma = \int_{\Gamma_\mathrm{N}} t_\mathrm{N} v \, \mathrm{d}\Gamma \quad \forall v \in \mathscr{U}^h \tag{14}$$

$$- \int_{\Gamma_\mathrm{D}}^{\mathrm{num}} \mu u^h \, \mathrm{d}\Gamma - \int_{\Gamma_\mathrm{D}}^{\mathrm{num}} k^{-1} \lambda^h \mu \, \mathrm{d}\Gamma = - \int_{\Gamma_\mathrm{D}}^{\mathrm{num}} \mu u_\mathrm{D} \, \mathrm{d}\Gamma \quad \forall \mu \in \mathscr{L}^h \tag{15}$$

The choice of the finite element subspaces and the integration of the Dirichlet boundary terms must satisfy the so-called inf–sup (or LBB) condition [20, 21]. In our case this condition imposes that there exists a positive constant α (independent of the characteristic size h of the elements) called the inf–sup value such that

$$\inf_{\lambda^h \in \mathscr{L}^h} \sup_{u^h \in \mathscr{U}^h} \frac{\int_{\Gamma_\mathrm{D}}^{\mathrm{num}} \lambda^h u^h \, \mathrm{d}\Gamma}{h^{1/2} \|\lambda^h\|_{0,\Gamma_\mathrm{D}} \|u^h\|_{1,\Omega}} \geqslant \alpha > 0 \tag{16}$$

where the 0 and 1 subscripts indicate L^2- and H^1-norms, respectively. The previous inequality is basically impossible to prove in practical situations. Fortunately, there exists a numerical inf–sup test [3]. This test reduces to the computation of eigenvalues for a sequence of meshes of increasing density. Let U_h and L_h be the vectors of potentials and Lagrange multipliers, respectively. The matrix problem corresponding to the variational form (15) is of the form

$$\begin{pmatrix} A_h & B_h^\mathrm{T} \\ B_h & -k^{-1} C_h \end{pmatrix} \begin{pmatrix} U_h \\ L_h \end{pmatrix} = \begin{pmatrix} F_h \\ D_h \end{pmatrix} \tag{17}$$

The inf–sup eigenproblem is the following (we use the energy matrix A_h instead of the H^1-norm matrix, assuming A_h is invertible):

$$\frac{1}{h} (B_h^\mathrm{T} C_h^{-1} B_h) V_h = \beta A_h V_h \tag{18}$$

Note the presence of the $1/h$ factor, inverse of the mesh size [21]. This is due to the fact that the Dirichlet constraint apply only to the boundary (in the case of an incompressible constraint which applies to the whole domain, the $1/h$ factor does not appear). We call β_p the first non-zero eigenvalue, then the value of α is simply $\sqrt{\beta_p}$. The inf–sup in practice reduces to the computation of α using meshes of increasing density. A sequence of three to four meshes is suggested in Reference [3]. Finally, as mentioned by Chapelle and Bathe, let us insist on the fact that, as valuable as this test may be, it can never be as valuable as definitive analytical proof. A method that can be shown to be BB-stable analytically will pass the numerical test but the reverse is not always true.

An equivalent numerical inf–sup test is given by the following eigenproblem:

$$\frac{1}{h}(B_h A_h^{-1} B_h^{\mathrm{T}}) W_h = \beta' C_h W_h \tag{19}$$

The first non-zero eigenvalue of (18) is the same as the first non-zero eigenvalue of (19). In practice, we shall solve the eigenproblem (19). If the inf–sup condition is satisfied, optimal rates of convergence are expected. We shall check these rates on three relative errors, namely the error in the 'energy' norm:

$$\varepsilon_{\Omega,\nabla u} = \left(\frac{\int_\Omega \nabla(u^h - u^{\mathrm{ex}}) \cdot \nabla(u^h - u^{\mathrm{ex}})\, \mathrm{d}\Omega}{\int_\Omega \nabla u^{\mathrm{ex}} \cdot \nabla u^{\mathrm{ex}}\, \mathrm{d}\Omega} \right)^{1/2} \tag{20}$$

the L^2 error norm measuring the accuracy of the Dirichlet boundary condition

$$\varepsilon_{\Gamma,u} = \left(\frac{\int_\Gamma (u^h - u^{\mathrm{ex}})^2\, \mathrm{d}\Gamma}{\int_\Gamma (u^{\mathrm{ex}})^2\, \mathrm{d}\Gamma} \right)^{1/2} \tag{21}$$

and, finally, the L^2 error norm on the Lagrange multiplier

$$\varepsilon_{\Gamma,\lambda} = \left(\frac{\int_\Gamma (\lambda^h - \nabla_n u^{\mathrm{ex}})^2\, \mathrm{d}\Gamma}{\int_\Gamma (\nabla_n u^{\mathrm{ex}})^2\, \mathrm{d}\Gamma} \right)^{1/2} \tag{22}$$

where ∇ is the gradient operator and ∇_n is its projection on the outward normal on the boundary.

2.2. Design of an adequate Lagrange multiplier space

The proper choice of the Lagrange multiplier space to impose Dirichlet boundary conditions has been studied in detail in Reference [1] within the standard finite element framework.

We consider problem (2) with exact solution (1).[¶] Dirichlet boundary conditions are imposed on the bottom part using continuous linear Lagrange multipliers. Nodal integration

[¶]To be precise, on the square shown in Figure 2, we did impose Dirichlet boundary conditions on the top part, by setting the field to zero there, thus rendering A_h invertible in (19).

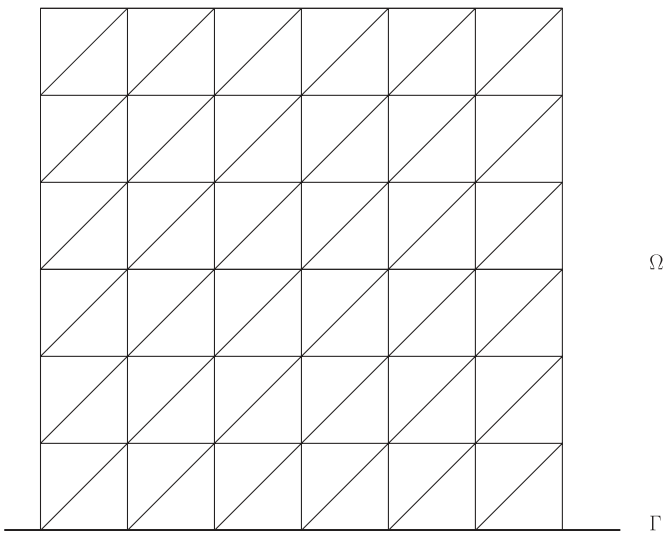

Figure 3. The unit-square model problem with a mesh matching the Dirichlet boundary.

(the integration points coincide with the nodes on each segment, each with equal weight) is used for all the integrals appearing in (15).

We build a sequence of four structured meshes with increasing density. One of them is shown in Figure 3. The convergence of the three exact errors are shown in Figure 4. From these results, it is clear (at least for this example) that no boundary locking occurs: the inf–sup parameter does not drop to zero and (as a consequence) the convergence rates are reasonable.

We carry the same computations to a sequence of non-interface-matching meshes. The unit-square of interest Ω is as usual the shaded area as shown in Figure 5. The most convenient choice for the Lagrange multiplier space is to take a linear continuous function along the segment of Γ. We shall denote this approach as the 'naive' approach. This choice was originally suggested by Dolbow *et al*. [22] for the treatment of frictional contact on an interface with an enriched basis and was again studied in Reference [16]. This yields a space of dimension 5 for the mesh shown in Figure 5 (left), corresponding to the five nodes ranging from A to E. The results obtained with this Lagrange multiplier space are given in Figure 6 for a nodal integration. It is clear from these results that locking occurs. The suboptimal convergence rate of the energy error denotes an over-constrained primal variable space. As shown in Reference [16], severe oscillations affect the Lagrange multiplier field (see Figure 7). The post-processing strategy proposed in Reference [16] allows, nevertheless, to obtain reasonable fluxes on the interface. Our goal is to build a Lagrange multiplier space, which could be used directly, for instance, within a contact algorithm.

To further illustrate why this 'naive' approach fails, we shall solve analytically the two-element scalar problem shown in Figure 8. The nodal forces F_1 and F_2 are supposed to model the action of the upper elements. The Lagrange multiplier space is discretized over Γ by a linear interpolation parametrized by the λ_1, λ_2 and λ_3 coefficients. The inner space is discretized with the four 'displacements' u_i, $i = 1, \ldots, 4$. The Lagrange multipliers

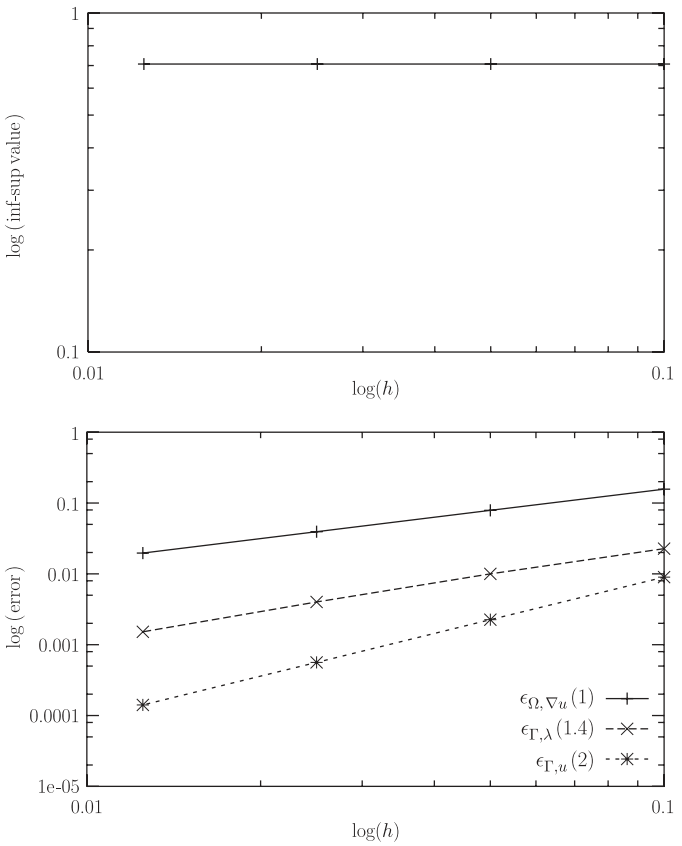

Figure 4. Results for structured matching meshes with nodal integration: inf–sup parameter and convergence of the errors. The rate of convergence is given for each curve.

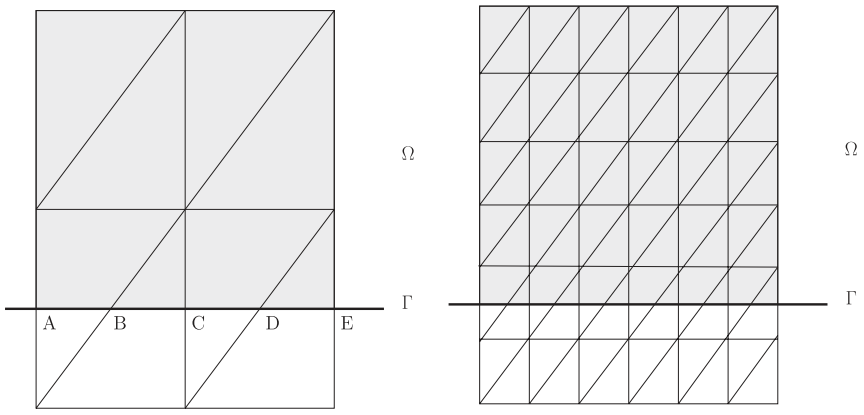

Figure 5. The first two meshes of a sequence of non-matching structured meshes.

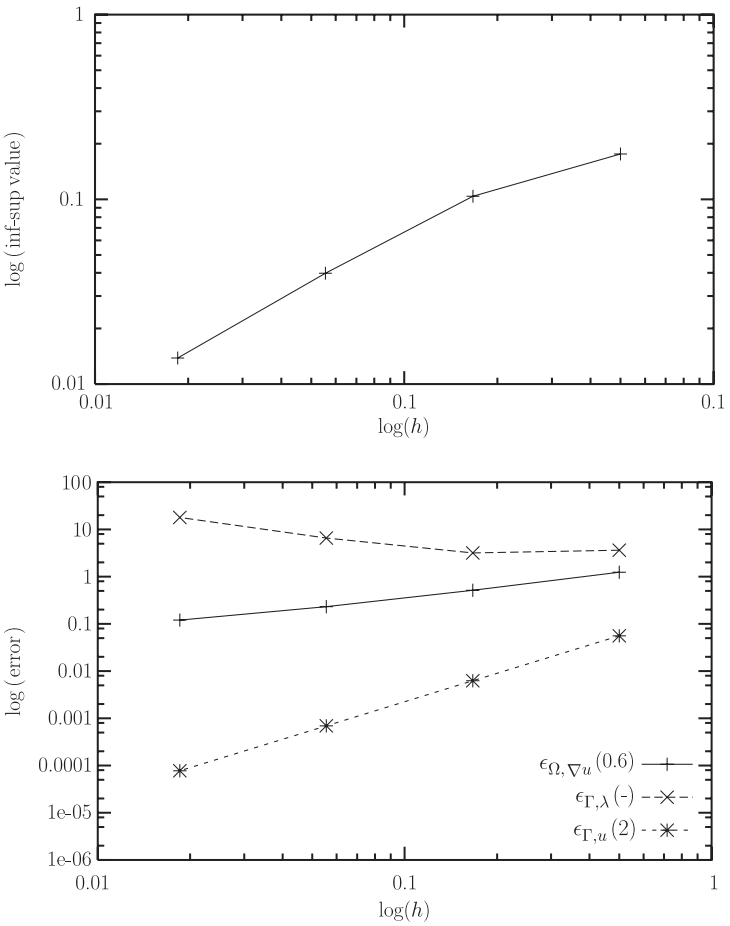

Figure 6. Results for non-matching structured meshes using a full Lagrange multiplier space: convergence of the errors and inf–sup parameter.

solution is

$$\lambda_1 = F \tag{23}$$

$$\lambda_2 = F + \frac{1}{(1-e)}[F] \tag{24}$$

$$\lambda_3 = F - \frac{1}{(1-e)^2}[F] \tag{25}$$

where $F = F_1 + F_2$ and $[F] = F_1 - F_2$. We observe that the second and third Lagrange multipliers become unbounded when the interface reaches the bottom layer of elements, especially λ_3 whose support drops to zero as e tends to one. Moreover, oscillations occur: the effect of $[F]$ is positive for λ_2 and negative for λ_3. Let us now try to reduce the Lagrange multiplier space

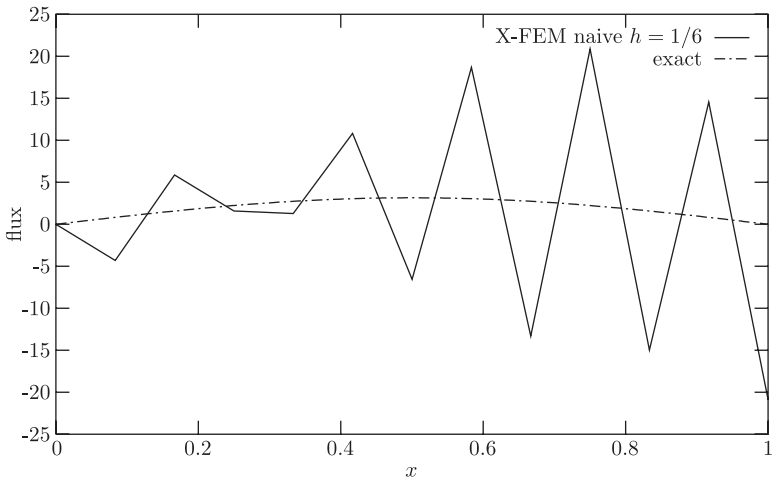

Figure 7. Exact and approximated flux with the naive X-FEM approach for the mesh shown in Figure 5 (right).

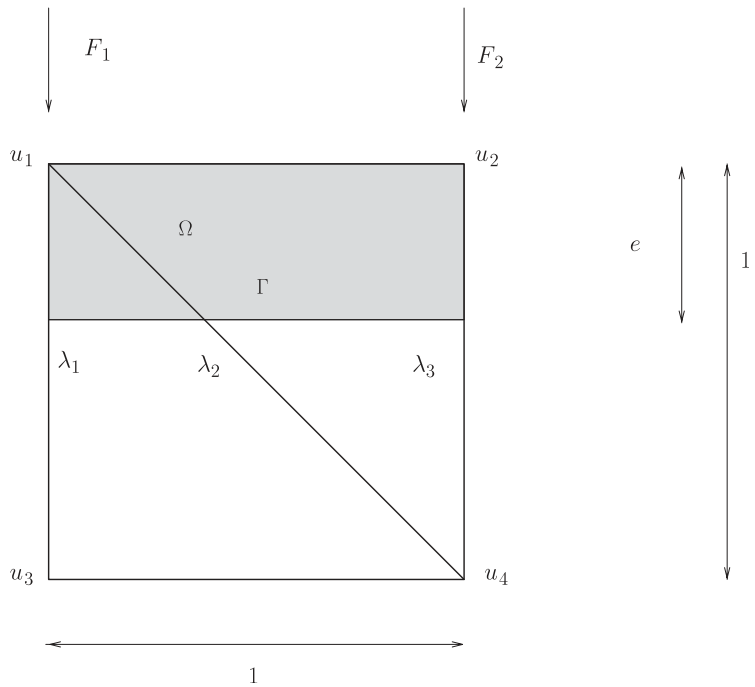

Figure 8. Two-element scalar problem.

to avoid spurious oscillations. If we set say $\lambda_2 = \lambda_3$, we obtain the Lagrange multiplier below which still exhibit oscillations.

$$\lambda_1 = F - \left(\frac{2e^3 - 9e^2 + 14e - 8}{4e^3 - 12e^2 + 7e + 4}\right)\left(\frac{1}{e}\right)[F] \tag{26}$$

$$\lambda_2 = F - \left(\frac{2e^2 - 5e + 4}{4e^3 - 12e^2 + 7e + 4}\right)[F] \tag{27}$$

$$\lambda_3 = \lambda_2 \tag{28}$$

On the other hand, if we set $\lambda_2 = (1 - e)\lambda_1 + e\lambda_3$ (linear variation over Γ), we obtain

$$\lambda_1 = F + \left(\frac{2e^3 - 8e^2 + 9e - 4}{4e^5 - 16e^4 + 28e^3 - 32e^2 + 17e - 4}\right)[F] \tag{29}$$

$$\lambda_2 = (1 - e)\lambda_1 + e\lambda_3 \tag{30}$$

$$\lambda_3 = F - \left(\frac{2e^3 - 8e^2 + 9e - 4}{4e^5 - 16e^4 + 28e^3 - 32e^2 + 17e - 4}\right)[F] \tag{31}$$

and the oscillations disappear.

This simple example shows that it may be possible to build an appropriate Lagrange multiplier space by shrinking the 'naive' space. We now need to design a strategy to automatically build this reduction for general meshes. These are the 'good' properties we are looking for:

- *Patch test*: The patch test of concern here is depicted in Figure 9. For any mesh in the rectangle, matching or not the interface Γ, the exact linear solution with constant flux must be recovered. A necessary condition is to be able to represent a constant Lagrange multiplier over Γ. Another necessary condition is that the integration rule over Γ must be exact for any linear field. By any linear field, we mean any piecewise continuous linear field, which can be represented over the segments composing Γ (for instance, 4 and 12 segments, respectively, for the mesh shown in Figure 6, left and right). Nodal integration over Γ does ensure this exact integration.
- *Stability with respect to the LBB*: The Lagrange multiplier space size must be small enough to pass the numerical inf–sup test but rich enough to preserve reasonable rates of convergence.
- *Stability with respect to the location of the boundary*: if the boundary is moved slightly (small changes in the level set values), we wish that the Lagrange multiplier space is only slightly perturbed. Also, if the boundary gets close to some nodes, we wish the Lagrange multipliers to remain finite. We wish to avoid the situation described by Equations (23)–(25) in which Lagrange multipliers blow up. This situation appears when the support of a multiplier vanishes.

In order to fulfil these requirements, we did use a trial and error approach. For every algorithm we would come up with, we checked the stability of the inf–sup parameter as well

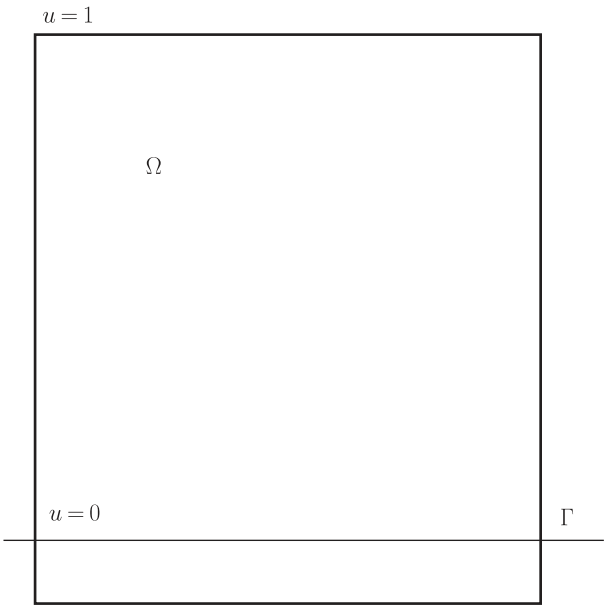

Figure 9. Illustration of the patch test.

as the smoothness of the Lagrange multiplier field. The algorithm selected is described below. It consists in building a set of winner nodes. The algorithm favours nodes close to the boundary or from which many edges that are intersecting the boundary emanate. The winner nodes selected by the algorithm are illustrated in Figure 10 for a straight and a circular boundary. Note that if the boundary is part of the mesh, the winner nodes are simply located on the boundary.

1. Place the nodes located exactly on the boundary (zero level set value) in W.
2. Place the edges cut by the boundary in S_e (i.e. the edges for which the product of the level set values at the vertices is strictly negative).
3. Place the nodes belonging to edges in S_e in S_n.
4. Compute the score of all nodes in S_n. The score of node i is given by a pair (n_i, l_i), n_i is the number of edges in S_e reaching node i and l_i is the opposite absolute value of the level set at node i:

$$\text{NodeScore}(i) = (n_i = \text{number of edges in } S_e \text{ reaching node } i, l_i = -|ls(i)|)$$

   where $ls(i)$ indicates the level set value at node i. The scores of two nodes may be compared in a lexicographic manner. Node i is 'better' than node j, if $n_i > n_j$. If $n_i = n_j$, then node i is better than node j if $l_i > l_j$. If $l_i = l_j$, the best node is the one with the highest identification number (or any other deterministic choice).
5. Compute the score of all edges in S_e. The score of the edge is a pair computed from the scores of its two nodes. Let i and j be these two nodes with i being better than j.

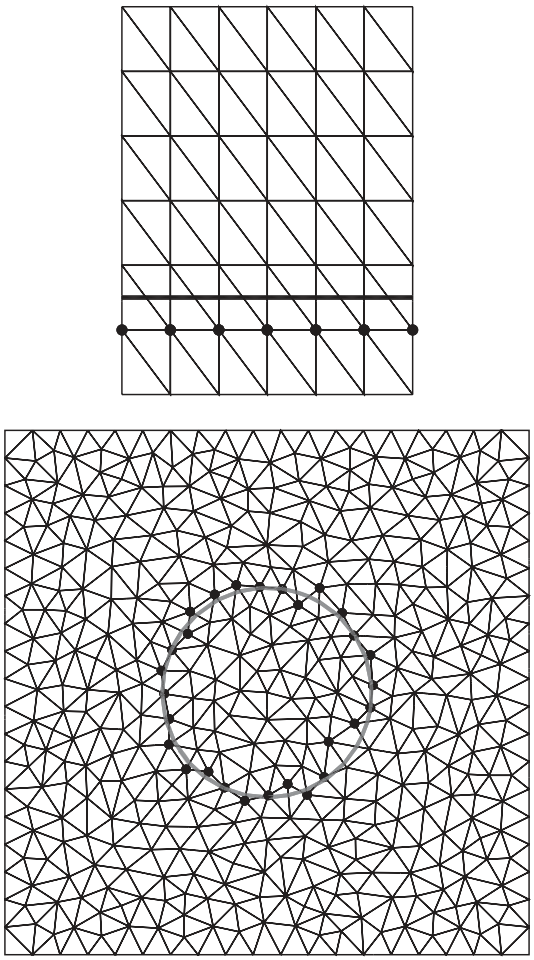

Figure 10. Winner nodes selected (thick node) by the algorithm and location of the iso-zero level set (thick line) for a straight (top) and a circular interface (bottom).

The score of the edge is given by

$$\text{EdgeScore}(e(i,j)) = (d_e = |n_i - n_j|, r_e = (l_i - l_j)/|l_i + l_j|) \tag{32}$$

As for the nodes, the scores of two edges may be compared in a lexicographic manner. An edge e is better than an edge f if $d_e > d_f$. If $d_e = d_f$, an edge e is better than an edge f if $r_e > r_f$. If $r_e = r_f$, the best edge is the one with the highest identification number.

6. Pick the best edge in S_e. Place its best node in W and remove it from S_n.
7. Remove the edges reaching the best node, just selected in step 6, from S_e.
8. If S_e is empty end the algorithm, otherwise go to step 4.

Once winner nodes have been selected, the Lagrange multiplier space may be built. The size of the multiplier space is the size of the winner nodes set W. This space is piecewise linear

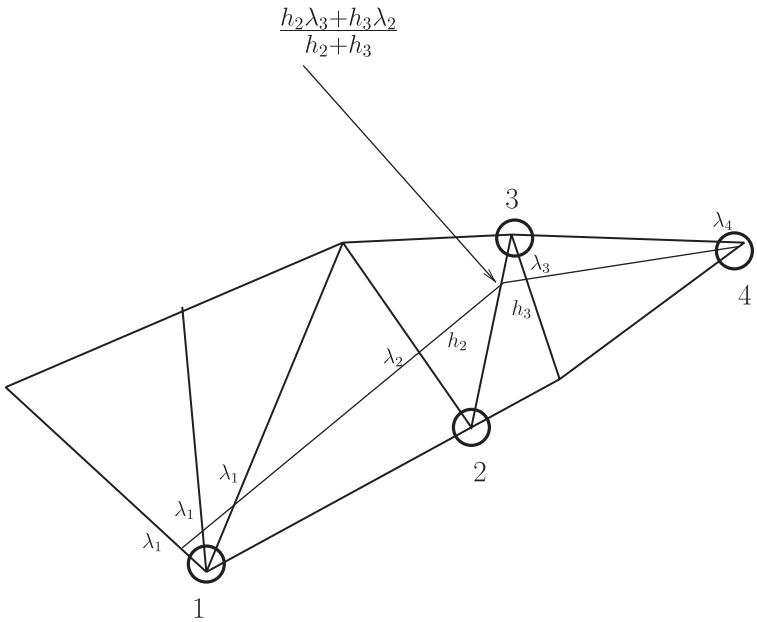

Figure 11. The Lagrange multiplier space on the boundary. The winner nodes are circled. The size of the space is 4.

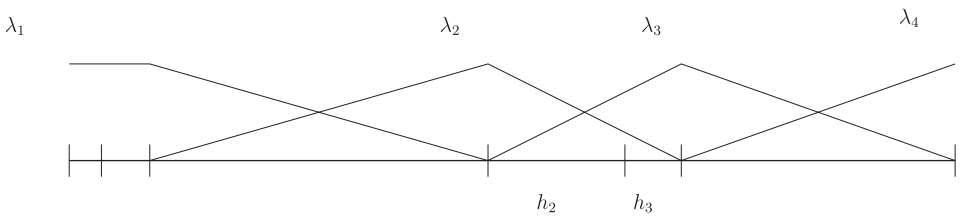

Figure 12. Representation of the shape functions for the Lagrange multiplier along the interface.

and continuous along the interface. The construction of the space is illustrated in Figure 11 where four winner nodes have been selected. On edges cut by the interface owning only one winner node, one degree of freedom attached to the winner node is created. If several edges cut by the interface emanate from the same winner node, they will share a common degree of freedom (as for λ_1 in Figure 11). On edges owning two winner nodes, the Lagrange multiplier is a linear combination of the Lagrange multipliers corresponding to those winner nodes. This linear combination is shown in Figure 11 in between the Lagrange multiplier λ_2 and λ_3. The lengths h_2 and h_3 denote the lengths of the interface segments within the elements.

Figure 12 illustrates the shape functions along the interface (each small vertical segment depicts an edge cut) and Figure 13 shows a possible distribution of the Lagrange multiplier.

We go back to the non-matching uniform mesh case whose results showed locking with the naive approach (Figure 6). The new results with the updated Lagrange multiplier space are

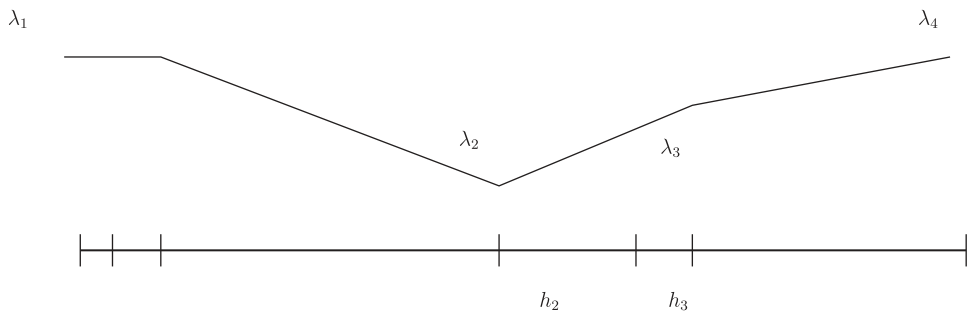

Figure 13. A possible distribution of the Lagrange multiplier value along the interface.

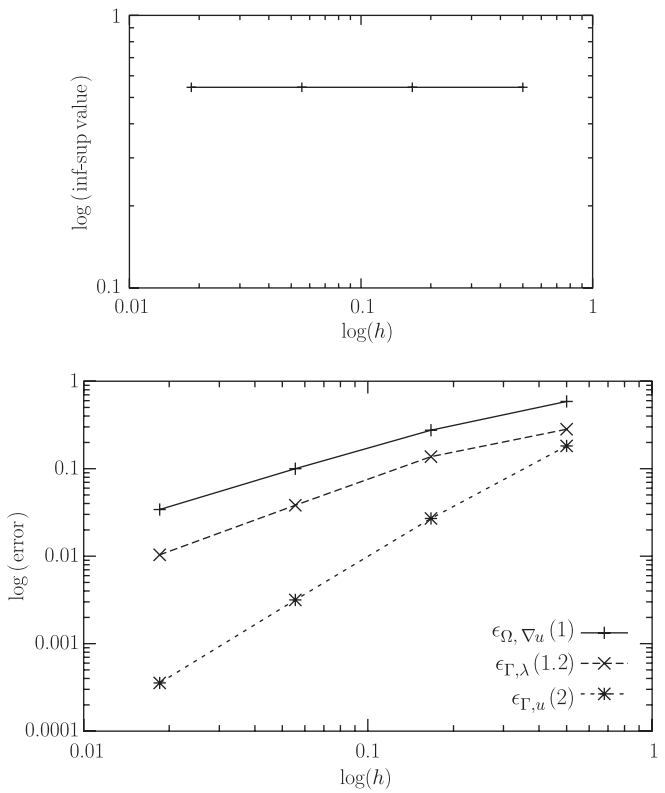

Figure 14. Results for non-matching (uniform) meshes using of the reduced multiplier space: inf–sup parameter and convergence of the errors.

shown in Figure 14. The locking is eliminated. We also checked a sequence of non-matching, non-uniform meshes shown in Figure 15. The results are given in Figure 16. The FEM results were obtained with a conforming unstructured mesh. It is interesting to note that the energy error is almost the same for the X-FEM and FEM computations as well as the error on the

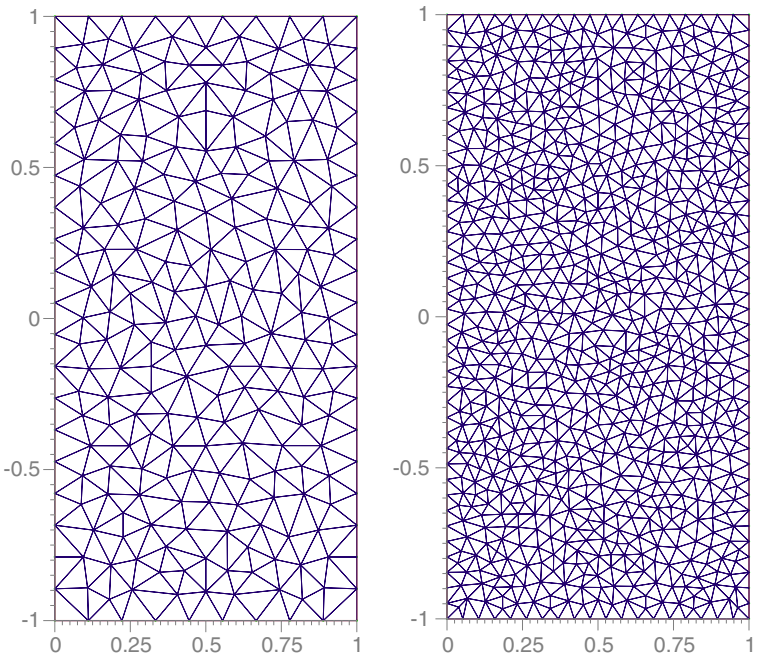

Figure 15. The first two meshes of a sequence of non-matching unstructured meshes. Only the upper half of the mesh is used for the computation.

enforcement of the Dirichlet constraint. The error on the Lagrange multiplier is slightly better for the FEM approach but the rates of convergence are similar. Finally, the Lagrange multiplier distribution along the interface is shown in Figure 17. Although mild oscillations are still present in the X-FEM computation (and only for the coarsest mesh), these oscillations bear nothing in common with the oscillations of the naive approach (Figure 7). In the last section of this paper, we shall use the non-locking Lagrange multiplier space to solve the resin transfer moulding process. But before, we wish to investigate the robustness of the present algorithm for the case of constraints on inner interfaces.

3. INTERFACIAL CONSTRAINTS

We consider an interface between two dissimilar materials shown in Figure 18. Each material is characterized by a material property α_i, $i = 1, 2$. The strong form of the equations on Ω_i, $i = 1, 2$ are

$$\begin{aligned} \nabla \cdot (\alpha_i \nabla u_i) &= 0 \quad && \text{on } \Omega_i \\ \alpha_i \nabla_{n_i} u_i &= t_{\mathrm{N}i} \quad && \text{on } \Gamma_{\mathrm{N}i} = \partial\Omega_i \Gamma \\ \alpha_i \nabla_{n_i} u_i &= \lambda_i \quad && \text{on } \Gamma \end{aligned} \tag{33}$$

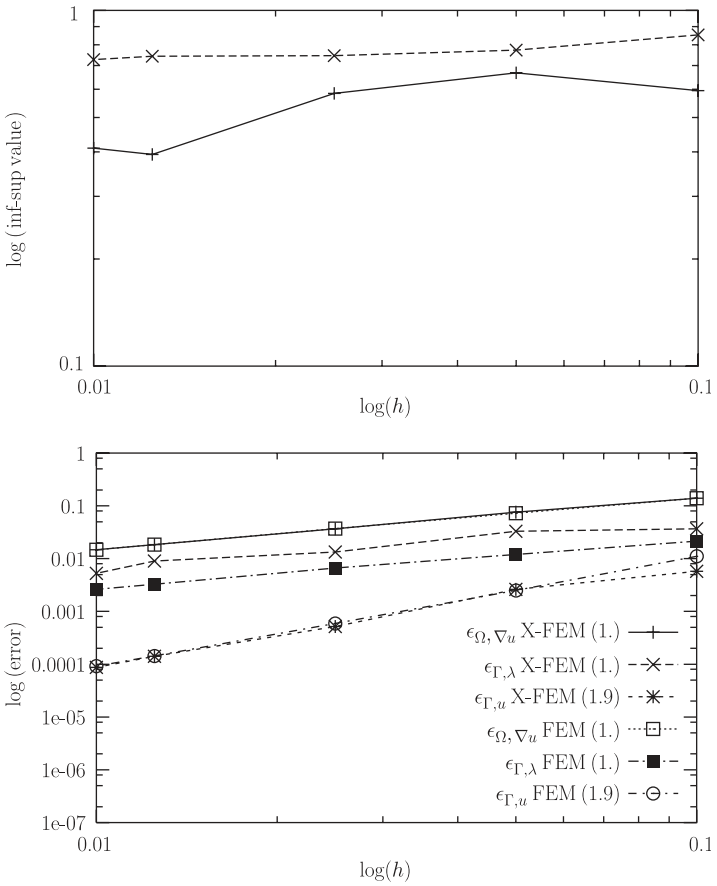

Figure 16. Results of convergence for non-matching, non-uniform meshes: inf–sup parameter (top) and errors (bottom).

where n_i is the outward normal to Ω_i. These equations are equivalent to the variational form:

$$\int_{\Omega_i} \alpha_i \nabla u_i \cdot \nabla v \, \mathrm{d}\Omega = \int_{\Gamma_{\mathrm{N}i}} t_{\mathrm{N}i} v \, \mathrm{d}\Gamma + \int_{\Gamma} \lambda_i v \, \mathrm{d}\Gamma \quad \forall v \in \mathscr{U}_i \tag{34}$$

where $\mathscr{U}_i$ are sets of 'regular enough' functions. Summing these two principles for $i = 1$ and $i = 2$, we obtain

$$\int_{\Omega} \alpha \nabla u \cdot \nabla v \, \mathrm{d}\Omega - \int_{\Gamma} \langle \lambda v \rangle \, \mathrm{d}\Gamma = \int_{\Gamma_{\mathrm{N}}} t_{\mathrm{N}} v \, \mathrm{d}\Gamma \quad \forall v \in \mathscr{U} \tag{35}$$

where

$$\Omega = \Omega_1 \cup \Omega_2, \quad \Gamma_{\mathrm{N}} = \Gamma_{\mathrm{N}1} \cup \Gamma_{\mathrm{N}2} \tag{36}$$

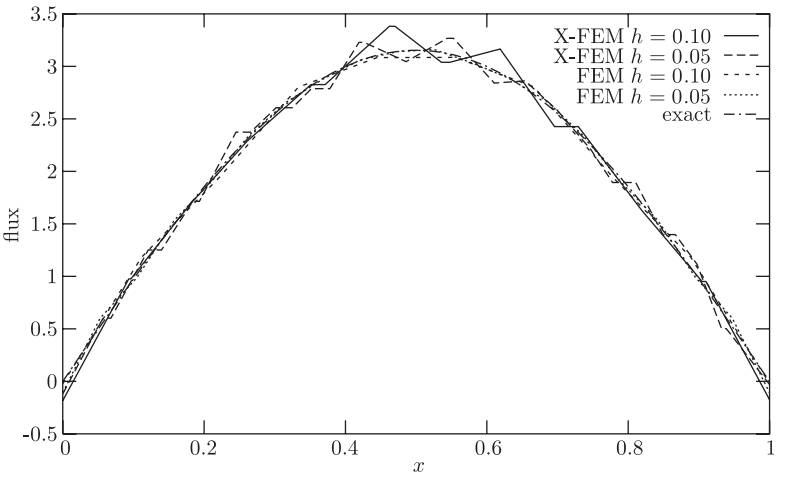

Figure 17. Exact and approximated fluxes on the boundary for a sequence of unstructured meshes.

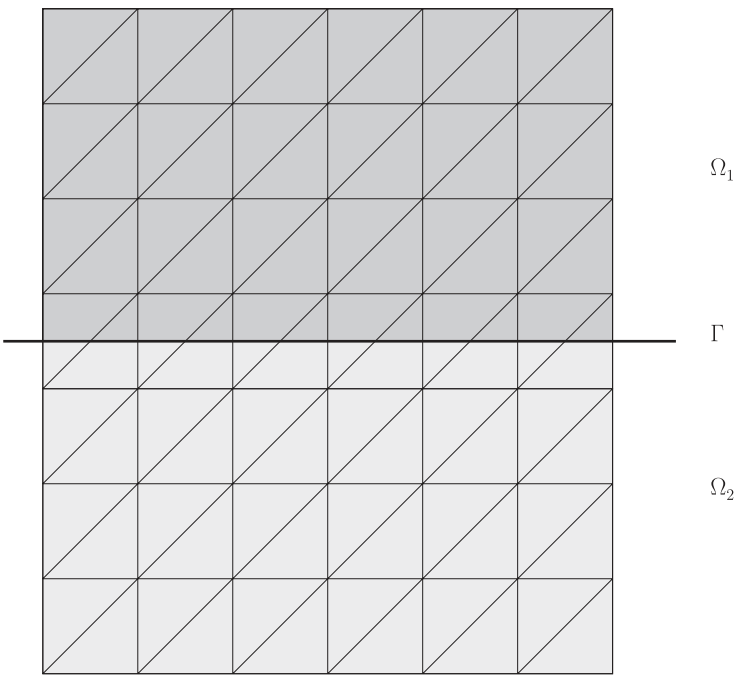

Figure 18. An interface Γ between two domains of interest Ω_1 and Ω_2.

and we have introduced the following compact notations:

- u and α represent the corresponding u_i and α_i on Ω_i, $i = 1, 2$;
- t_{N} represents the corresponding $t_{\mathrm{N}i}$ on $\Gamma_{\mathrm{N}i}$, $i = 1, 2$;

- $\mathscr{W}$ is the union of the spaces $\mathscr{W}_1$ and $\mathscr{W}_2$. This space allows for discontinuous functions along Γ; and
- $\langle \lambda v \rangle = \lambda_1 v_1 + \lambda_2 v_2$;

Regarding the interfacial condition on Γ, we consider two important practical cases: continuous primal field ($u_1 = u_2$) and flux 'equilibrium' ($\lambda_1 + \lambda_2 = 0$). In the first case the interface condition reads

$$u_1 - u_2 = 0, \quad \frac{u_1 + u_2}{2} = -b(\lambda_1 + \lambda_2) + \overline{u} \quad \text{on } \Gamma \tag{37}$$

and in the second case

$$\lambda_1 + \lambda_2 = 0, \quad \frac{\lambda_1 - \lambda_2}{2} = -k(u_1 - u_2) + \overline{t} \quad \text{on } \Gamma \tag{38}$$

where b, $\overline{u}$, k and $\overline{t}$ are physical interface parameters.

Constraint (37) is representative of the interface condition on the heat flux (λ) in a phase-transformation problem in which the temperature u is continuous on the front [14]. It also represents the condition on the interface between a collapsed and swollen phase in the modelling of stimulus-responsive hydrogels [16] where the chemical potential u is continuous at the interface and the lack of equilibrium of the flux is related to the speed of the front. In the limiting case of $b \to 0$, we obtain two decoupled problems on Ω_1 and Ω_2 with a Dirichlet condition $\overline{u}$ on Γ. In the limiting case of $b \to \infty$, we obtain a perfectly 'bonded' interface: continuity of flux and primal variable.

Constraint (38) is representative of two elastic media bonded with a spring of stiffness k as well as two different conductive media glued together with an interface of conductivity k. In the limiting case of $k \to 0$, we obtain two decoupled problems on Ω_1 and Ω_2 with a Neumann condition $\overline{\lambda}$ on Γ. In the limiting case of $k \to \infty$, we obtain a perfectly 'bonded' interface: continuity of flux and primal variable.

Our goal is to obtain discrete robust X-FEM settings in the important practical cases of k big (stiff or fully bonded interface) or b small. (The case of k small does not require a two-field formulation and the case of b big leads to a two-field formulation similar to the case of k big.)

3.1. Parameter k big

This case corresponds to a stiff spring. We decide to satisfy *a priori* the condition $\lambda_1 + \lambda_2 = 0$, i.e. $\lambda_2 = -\lambda_1$ and $\langle \lambda v \rangle = \lambda_1 (v_1 - v_2) = \lambda_1 [v]$. We are left with two relations (34) and (38) from which we build the following two-field variational principle:

$$\int_\Omega \alpha \nabla u \cdot \nabla v \, \mathrm{d}\Omega - \int_\Gamma \lambda_1 [v] \, \mathrm{d}\Gamma = \int_{\Gamma_N} \lambda_N v \, \mathrm{d}\Gamma \quad \forall v \in \mathscr{W} \tag{39}$$

$$-\int_\Gamma [u] \mu_1 \, \mathrm{d}\Gamma - \int_\Gamma k^{-1} \lambda_1 \mu_1 \, \mathrm{d}\Gamma = -\int_\Gamma k^{-1} \overline{t} \mu_1 \, \mathrm{d}\Gamma \quad \forall \mu_1 \in \mathscr{L} \tag{40}$$

The Lagrange multiplier space is discretized as explained in Section 2.2. The matrix problem is of the same form as (17). In order to show the robustness of the above variational principle and choice of the Lagrange multiplier space, we consider a perfectly bonded material interface

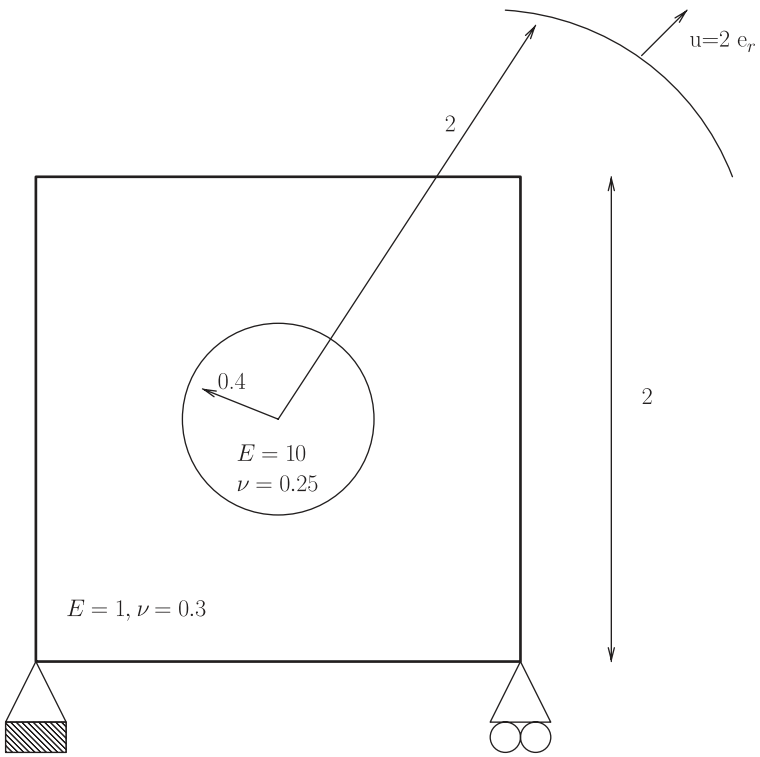

Figure 19. An inclusion problem. The inclusion has a Young modulus of 10 and Poisson ratio of 0.25, and the matrix has a Young modulus of 1 and Poisson ratio of 0.3.

problem ($k = \infty$) shown in Figure 19. The exact solution corresponds to a radial displacement of amplitude 2 imposed at a distance of 2 from the inclusion centre. This problem was already considered in References [9, 10]. Note that since this example is vectorial and not scalar, the above variational form must be adapted (α is the fourth-order elasticity tensor, u is the displacement field, λ is the traction vector on the interface for which both x and y components are discretized).

The inf–sup parameter is shown in Figure 20 for a sequence of meshes both for conforming (FEM) and non-conforming meshes (X-FEM). The formulation appears to pass numerically the patch test. The corresponding error on the Lagrange multiplier are plotted in Figure 21. These convergence are as good for the FEM and X-FEM cases. The convergence of the energy error is shown in Figure 22. We did add on this graph two other curves: the X-FEM case with a ridge enrichment (and no use of Lagrange multiplier, see Reference [10]) and X-FEM results with a naive Lagrange multiplier space. In the latter case, the error is an order of magnitude higher and the corresponding Lagrange multipliers do not converge (the error on the Lagrange multiplier was not plotted in Figure 21 because they are above 100%). Finally, Figure 23 gives the distribution along a quarter of the interface of the pointwise error of the Lagrange multiplier for the FEM and X-FEM case and two different meshes. The error decreases as the mesh is refined.

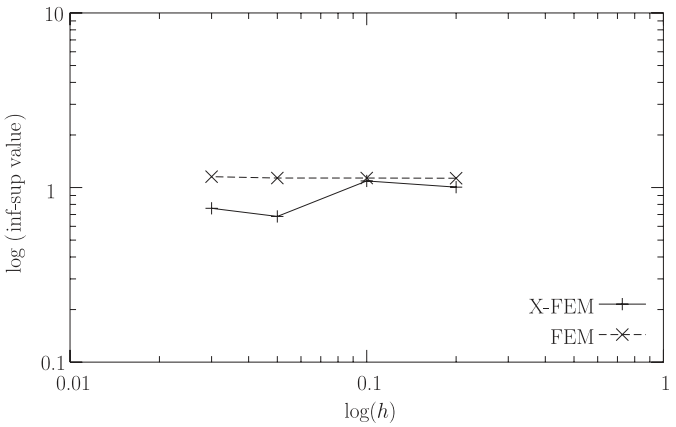

Figure 20. Inf–sup parameter for the material interface problem.

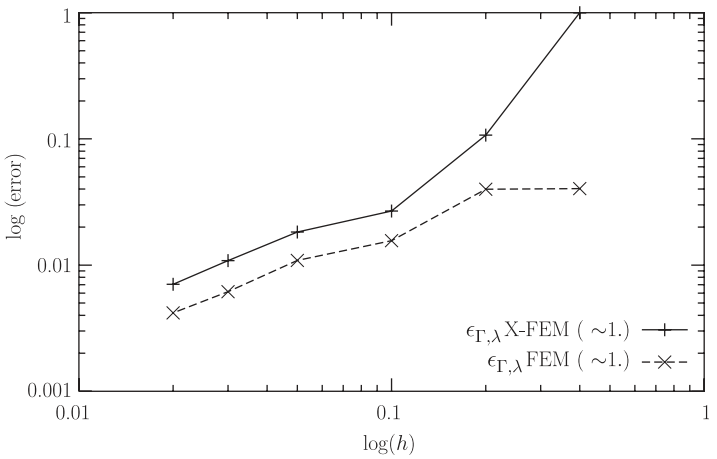

Figure 21. Convergence of the L^2 error on the Lagrange multiplier for the material interface problem.

3.2. Parameter b small

In this case, we consider the following three-field formulation:

$$\int_\Omega \alpha \nabla u \cdot \nabla v \, \mathrm{d}\Omega - \int_\Gamma \langle \lambda v \rangle \, \mathrm{d}\Gamma = \int_{\Gamma_N} t_N v \, \mathrm{d}\Gamma \quad \forall v \in \mathscr{U} \tag{41}$$

$$-\int_\Gamma \langle \mu u \rangle \, \mathrm{d}\Gamma - \int_\Gamma b \langle \mu \rangle \langle \lambda \rangle \, \mathrm{d}\Gamma = -\int_\Gamma \langle \overline{u} \mu \rangle \, \mathrm{d}\Gamma \quad \forall \mu_1, \quad \mu_2 \in \mathscr{L} \tag{42}$$

In order to show the effectiveness of this formulation, we consider a phase-transition problem taken from Reference [16]. The geometry and data of the problem are described in Figure 24.

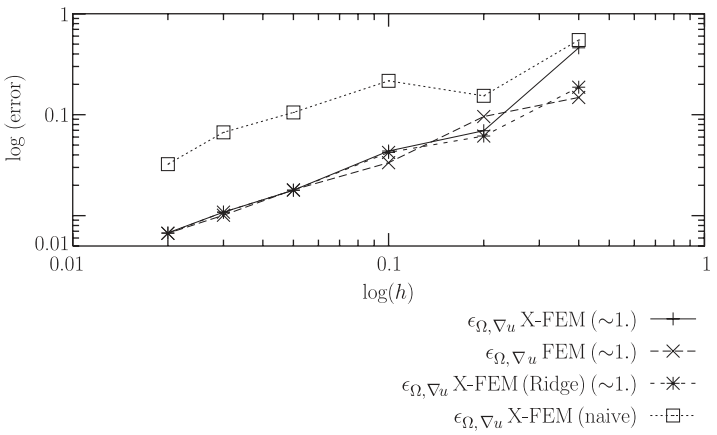

Figure 22. Convergence of the energy norm for the material interface problem.

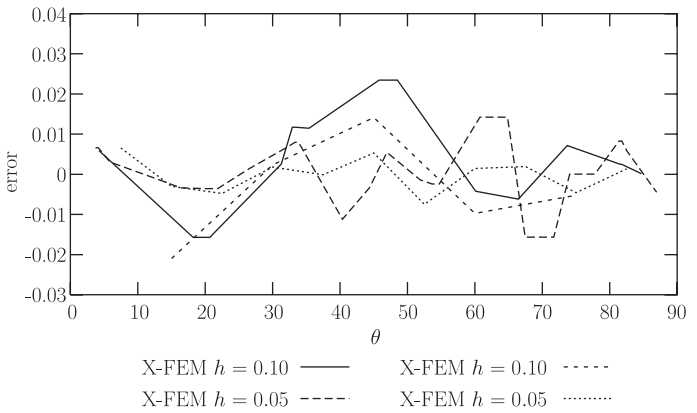

Figure 23. Error on the norm of the Lagrange multiplier for two conforming (FEM) and two non-conforming meshes (X-FEM).

The energy error and interface error are drawn in Figure 25 in the FEM (conforming mesh) and X-FEM cases, for a parameter (mobility) $b = 0.0$. In both cases, the meshes considered are unstructured. The interface error is given by

$$\varepsilon_{\Gamma,\langle\lambda\rangle} = \left(\frac{\int_\Gamma (\langle\lambda^h\rangle - \langle\lambda^{\text{ex}}\rangle)^2 \, \mathrm{d}\Gamma}{\int_\Gamma (\langle\lambda^{\text{ex}}\rangle)^2 \, \mathrm{d}\Gamma} \right)^{1/2} \tag{43}$$

We observe a similar behaviour of the FEM and the X-FEM. Again the X-FEM fluxes are a bit less accurate than the FEM ones, but they both converge at about the same rate.

Finally, we give in Figure 26, the influence of mobility b on the error on the interface, $\varepsilon_{\Gamma,\langle\lambda\rangle}$. The X-FEM and FEM follow the same trend, the error is higher as the problem becomes stiffer, $b = 0.0$ being the stiffest case.

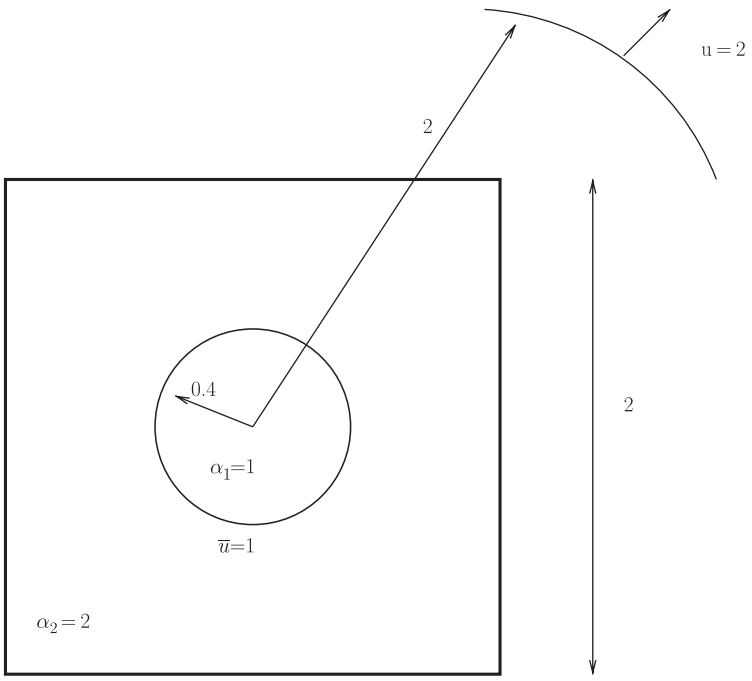

Figure 24. Geometry of the phase-transformation problem.

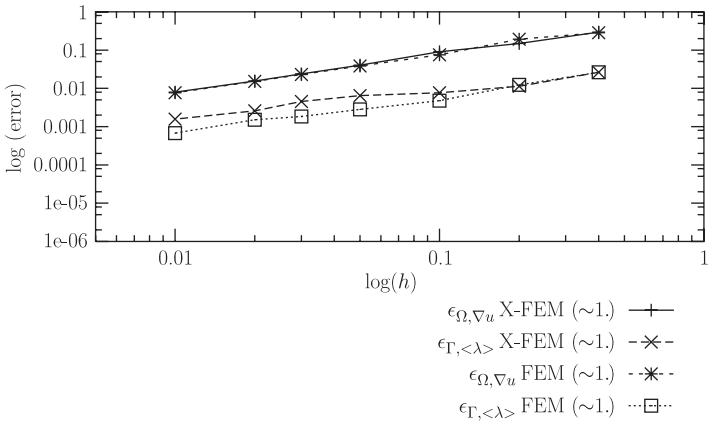

Figure 25. Convergence of the errors for the phase-transformation problem.

4. APPLICATION TO THE RESIN TRANSFER MOULDING PROCESS

Section 2 did suggest a coherent Lagrange multiplier space to impose Dirichlet boundary conditions on a boundary not necessarily matched by the mesh. The approach showed robust

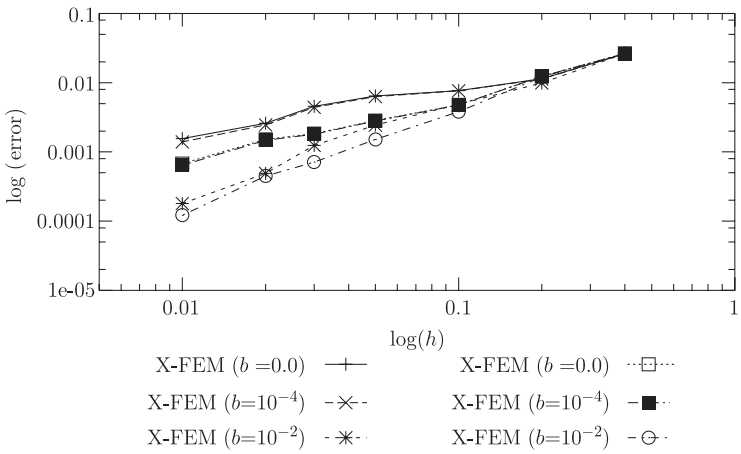

Figure 26. Impact of the mobility on the convergence of the interface error $\varepsilon_{\Gamma,\langle\lambda\rangle}$.

results on a benchmark problem. We now proceed to a more complex application involving a moving Dirichlet condition.

Resin transfer moulding (RTM) is a specialized process for bulk composites manufacturing. The idea is to inject a low-viscosity resin in a rigid mould already containing reinforcements. This reinforcement is usually made of layers of fibrous material (carbon or glass fibres), and has been placed in the mould before injection by an appropriate operation. The reinforcement is porous and allows for the resin to percolate through the voids and ultimately fill the mould; as for a regular thermoplastic moulding process. In previous studies Bechet *et al*. [23, 24] proposed a level set approach to discretize the interface which was proved to be very flexible, and allowed to break up the minimal time step (CFL) barrier for a given simulation while still obtaining accurate results. However, the boundary condition (in that case, null pressure) still requested remeshing in order to appear accurately in the model. In the target physical model (non-isothermal RTM simulation), this remeshing was necessary to avoid numerical dissipation near the front. Of course, this is not the case always, and for the sake of robustness and computational efficiency, it is generally better to avoid remeshing whenever possible. We demonstrate here that it is possible to have a very natural representation of the flow front within a fixed mesh; which is indeed not the case using common 'volume of fluid' approaches [25, 26]. The experimental setting is entirely from Reference [23], but we shall recall it here for the sake of completeness. We only performed additional simulations with a different numerical model in order to show good agreement with older models and experiments.

4.1. Mechanical model

The fluid motion in an isothermal resin transfer moulding process is governed by Darcy's law, which is linear and leads to elliptic problems. In a porous media, Darcy's law relates Darcy's velocity $\mathbf{v}_d$ to pressure p of the fluid via the permeability tensor $\mathbf{K}$ and the dynamic

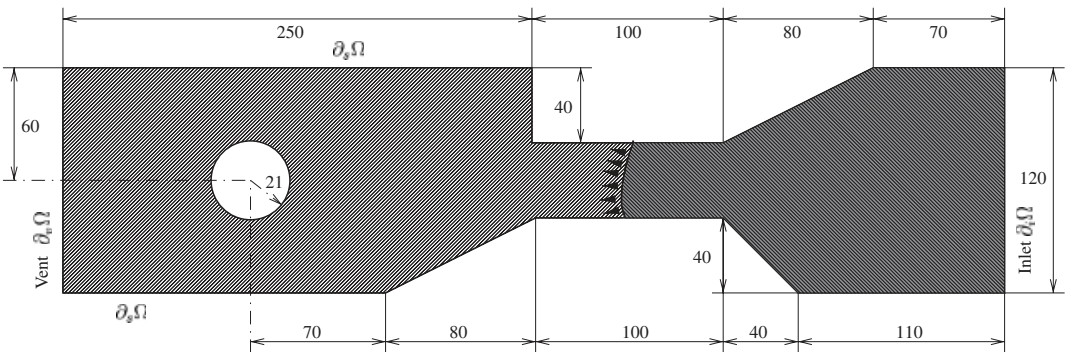

Figure 27. Mould geometry. Dimensions are in mm.

viscosity μ:

$$\mathbf{v}_d = -\frac{\mathbf{K}}{\mu} \cdot \nabla p \tag{44}$$

Darcy's velocity $\mathbf{v}_d$ in Equation (44) is related to the effective particle velocity $\mathbf{v}_e$ of the fluid in the porous media via the porosity ϕ of the media. The latter is lower than 1.0, in consequence the effective velocity is always greater than Darcy's velocity:

$$\mathbf{v}_e = \frac{\mathbf{v}_d}{\phi} \tag{45}$$

It should be noted that the local flow front velocity in the case of a free surface flow is $\mathbf{v}_e$. The conservation of mass yields:

$$\nabla \cdot \left(\frac{\mathbf{K}}{\mu} \cdot \nabla p \right) = 0 \tag{46}$$

If $\mathbf{K}$ and μ are constants, it can be simplified into

$$\Delta p = 0 \tag{47}$$

In real moulds, this is seldom the case; the reinforcement is usually not the same everywhere and curing effects in the resin changes its viscosity, with effects both in time and space.

4.2. Mould geometry

The mould shown in Figure 27 is a planar cavity with the resin inlet at the right side, and the vent on the left side. It features several obstacles (narrowing channel, widening area and insert) to mimic typical geometries coming from industrial moulds.

4.3. Boundary conditions and material properties

We deal here with a free surface flow, and boundary conditions are the following. The wet part of the mould is identified as Ω_w, and the dry part as Ω_d. We have at any instant $\Omega_w + \Omega_d = \Omega$, the total volume of the mould. Let the sides of the mould be noted $\partial_s\Omega$, the vent $\partial_v\Omega$ and the inlet $\partial_i\Omega$. On the walls of the mould as well as along inserts, a perfect slip condition is

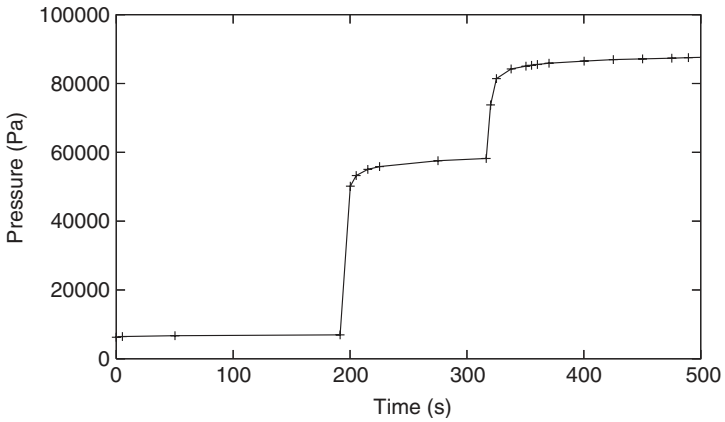

Figure 28. Resin-injection pressure.

expected. In the finite element framework, this means no specific treatment; it is a Neumann condition with zero-flux:

$$\nabla p \cdot \mathbf{n} = 0 \quad \text{on } \partial_s \Omega \tag{48}$$

On the free surface, we apply the atmospheric pressure via the vent. The air has a much lower viscosity than the resin, so there is no significant pressure difference between the vent and the current front position. The boundary condition is applied directly at the front position. Note that the air side does not generate any additional degrees of freedom so only the nodes for which the support covers some resin are activated as in Reference [11]. Differential pressure measurements are made, so the condition is homogeneous:

$$p = 0 \quad \text{on } \partial\Omega_d \cap \partial\Omega_w \tag{49}$$

This is the Dirichlet boundary condition that must be specifically treated because its application area $\partial\Omega_d \cap \partial\Omega_w$ crosses element boundaries. At the inlet, one impose another Dirichlet boundary condition, although in a regular manner, as no mesh elements are crossed (this boundary condition is part of the mesh). The resin-injection pressure $p_i(t)$ is applied here. It is not constant and should be driven over time.

$$p = p_i(t) \quad \text{on } \partial_i \Omega \tag{50}$$

The experiment was done without any precise control over the pressure. It was rather directly measured at the inlet gate and recorded along with the front position at specific time steps. It is this time-dependent pressure that we will use in our model. Figure 28 shows the time dependence of p_i.

Material properties are the following:

- The viscosity of the resin is $\mu = 0.1\,\text{Pa s}$.
- The permeability of the reinforcement is $K = 5.2 \times 10^{-10}\,\text{m}^2$; it is considered as an isotropic fabric so the permeability tensor is $\mathbf{K} = K \cdot \mathbf{I}$.
- The porosity of the reinforcement is $\phi = 0.71$.

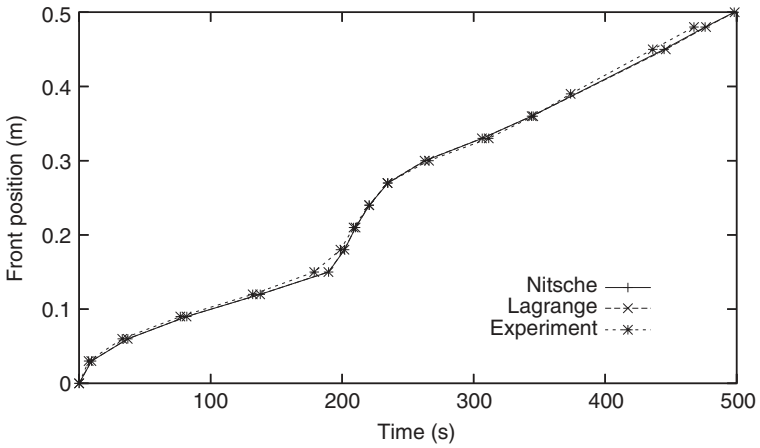

Figure 29. Front position.

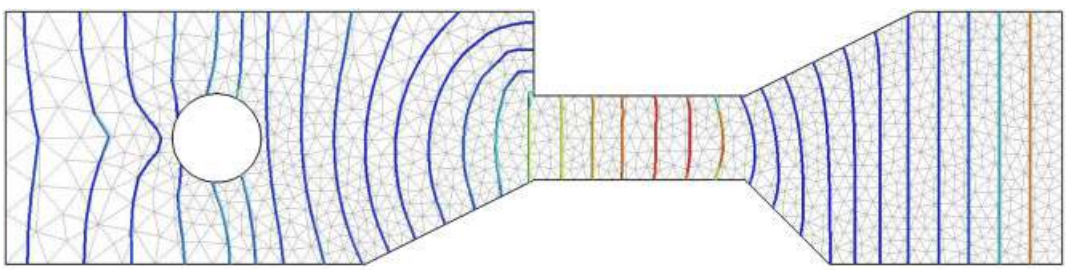

Figure 30. Successive flow front positions and mesh.

4.4. Simulation results and comparison with previous studies

We present in the sequel numerical results based on two approaches to enforce the boundary condition (a) with Nitsche's approach [17] and (b) with Lagrange multipliers as discussed in previous sections. In Figure 29, a very good agreement is observed with previous experimental results for both methods. For the sake of conciseness, we do not show images of the experiment, those can be viewed in Reference [23]. We then show successive flow front positions and the related mesh used to compute the filling in Figure 30. The front is smooth (as far as the mesh can handle), and the boundary condition weakly enforced with Lagrange multipliers in that case. We did not present the same results for Nitsche's approach as they are very close. One can see in Figure 29 that the results for Lagrange multipliers and Nitsche's method are indistinguishable. In addition, for Lagrange multipliers, there is no need to determine an adequate regularization parameter as in Nitsche's method. The Nitsche's parameter for the simulation above was computed from the eigenvalue problem described in Reference [4] based on the initial resin front location. The parameter was then kept constant for the whole simulation. The proper choice of the Nitsche parameter is important. Indeed, a bad parameter leads in general to poor quality solutions (see Reference [4] for square Laplacian problems on uniform grids in

the mesh-free context). Our experience with non-uniform grids in the finite element context confirms the results of Fernández-Méndez and Huerta [4]. We found that the proper Nitsche parameter depends not only on the mesh size, but also on the mesh topology.

5. CONCLUSIONS

The imposition of Dirichlet or interface conditions in the X-FEM context must be handled with care. We showed on simple examples and with more elaborate tools (numerical inf–sup and convergence rate) that the naive Lagrange multiplier space on the boundary (interface) leads to locking. There are two classical ways to go around the locking problem: either reduce the Lagrange multiplier space or 'enrich' the primal field. We used the first approach in this paper to carefully craft a non-locking Lagrange multiplier space for 2D triangular meshes. The approach showed satisfactory results for Dirichlet as well as for inner interfacial constraints. Finally, a 2D moving Dirichlet front showed the robustness of the approach in a less academic setting (resin transfer moulding process).

Current efforts are focused on 3D and any types of elements as well as non-linear constraints such as contact. These efforts will be the subject of a forthcoming paper.

ACKNOWLEDGEMENTS

The support of the French Ministry of Research (ACI program) is gratefully acknowledged. We are also grateful to Antonio Huerta and John Dolbow for fruitful discussions.

REFERENCES

1. Babuška I. The finite element method with Lagrangian multipliers. *Numerische Mathematik* 1973; **20**:179–192.
2. Barbosa H, Hughes T. Finite element method with Lagrange multipliers on the boundary. Circumventing the Babuska–Brezzi condition. *Computer Methods in Applied Mechanics and Engineering* 1991; **85**(1): 109–128.
3. Chapelle D, Bathe KJ. The inf–sup test. *Computers and Structures* 1993; **47**:537–545.
4. Fernández-Méndez S, Huerta A. Imposing essential boundary conditions in mesh-free methods. *Computer Methods in Applied Mechanics and Engineering* 2004; **193**:1257–1275.
5. Belytschko T, Lu Y, Gu L. Element-free Galerkin methods. *International Journal for Numerical Methods in Engineering* 1994; **37**:229–256.
6. Babuška I, Melenk I. Partition of unity method. *International Journal for Numerical Methods in Engineering* 1997; **40**(4):727–758.
7. Belytschko T, Black T. Elastic crack growth in finite elements with minimal remeshing. *International Journal for Numerical Methods in Engineering* 1999; **45**(5):601–620.
8. Moës N, Dolbow J, Belytschko T. A finite element method for crack growth without remeshing. *International Journal for Numerical Methods in Engineering* 1999; **46**:131–150.
9. Sukumar N, Chopp DL, Moës N, Belytschko T. Modeling holes and inclusions by level sets in the extended finite element method. *Computer Methods in Applied Mechanics and Engineering* 2001; **190**:6183–6200.
10. Moës N, Cloirec M, Cartraud P, Remacle J-F. A computational approach to handle complex microstructure geometries. *Computer Methods in Applied Mechanics and Engineering* 2003; **192**:3163–3177.
11. Daux C, Moës N, Dolbow J, Sukumar N, Belytschko T. Arbitrary branched and intersecting cracks with the eXtended Finite Element Method. *International Journal for Numerical Methods in Engineering* 2000; **48**:1741–1760.
12. Gravouil A, Moës N, Belytschko T. Non-planar 3D crack growth by the extended finite element and level sets. Part II: level set update. *International Journal for Numerical Methods in Engineering* 2002; **53**:2569–2586.

13. Ji H, Chopp D, Dolbow JE. A hybrid extended finite element/level set method for modeling phase transformations. *International Journal for Numerical Methods in Engineering* 2002; **54**:1209–1233.
14. Chessa J, Smolinski P, Belytschko T. The extended finite element method (X-FEM) for solidification problems. *International Journal for Numerical Methods in Engineering* 2002; **53**:1959–1977.
15. Merle R, Dolbow J. Solving thermal and phase change problems with the extended finite element method. *Computer Methods in Applied Mechanics and Engineering* 2002; **28**(5):339–350.
16. Ji H, Dolbow J. On strategies for enforcing interfacial constraints and evaluating jump conditions with the extended finite element method. *International Journal for Numerical Methods in Engineering* 2004; **61**:2508–2535.
17. Nitsche J. Ber ein variationsprinzip zur lsung von dirichlet-problemen bei vervendung von teilrumen, die keinen randbedingungen unterworfen sind. *Abhandlungen aus dem Mathematischen Seminaren des Universitt Hamburg* 1970; **36**:9–15.
18. Hansbo A, Hansbo P. An unfitted finite element method, based on Nitsche's method, for elliptic interface problems. *Computer Methods in Applied Mechanics and Engineering* 2002; **191**:5537–5552.
19. Hansbo A, Hansbo P. A finite element method for the simulation of strong and weak discontinuities in solid mechanics. *Computer Methods in Applied Mechanics and Engineering* 2004; **193**:3523–3540.
20. Brezzi F, Fortin M. *Mixed and Hybrid Finite Element Methods*. Springer Series in Computational Mathematics. Springer: Berlin, 1991.
21. El-Abbasi N, Bathe K. Stability and patch test performance of contact discretizations and a new algorithm. *Computers and Structures* 2001; **79**:1473–1486.
22. Dolbow J, Moës N, Belytschko T. An extended finite element method for modeling crack growth with frictional contact. *Computer Methods in Applied Mechanics and Engineering* 2001; **190**:6825–6846.
23. Béchet E, Ruiz E, Trochu F, Cuillière J. Remeshing algorithms applied to mould filling simulations in resin transfer moulding. *Journal of Reinforced Plastics and Composites* 2003; **23**:17–37.
24. Béchet E, Ruiz E, Trochu F, Cuillière J. Adaptive mesh generation for mould filling problems in resin transfer moulding. *Composites* 2003; **34**(Part A):813–834.
25. Bruschke M, Advani S. A finite element/control volume approach to mould filling in anisotropic porous media. *Polymer Composites* 1990; **11**:398–405.
26. Trochu F, Gauvin R, Gao D. Numerical analysis of the resin transfer moulding process by the finite element method. *Advances in Polymer Technology* 1993; **12**:329–342.